PAPER • OPEN ACCESS

Metal–insulator transition in composition-tuned nickel oxide films

View the article online for updates and enhancements.

OPEN ACCESS

IOP Publishing

Metal–insulator transition in composition-tuned nickel oxide films

Jennifer Fowlie[1,*] , Alexandru B Georgescu[2], Andreas Suter[3], Bernat Mundet[4,5],
Constance Toulouse[6] , Nicolas Jaouen[7] , Michel Viret[8], Claribel Domínguez[4],
Marta Gibert[9], Zaher Salman[3], Thomas Prokscha[3], Duncan T L Alexander[5] ,
Jens Kreisel[6], Antoine Georges[4,10,11,12], Andrew J Millis[10,13] and Jean-Marc Triscone[4]

[1] Department of Applied Physics, Stanford University, Stanford, CA, United States of America
[2] Department of Materials Science and Engineering, Northwestern University, Evanston, IL, United States
of America
[3] Laboratory for Muon-Spin Spectroscopy, Paul Scherrer Institute, Villigen PSI, Switzerland
[4] Department of Quantum Matter Physics, University of Geneva, Geneva, Switzerland
[5] Electron Spectrometry and Microscopy Laboratory (LSME), Institute of Physics (IPHYS), École
Polytechnique Fédérale de Lausanne (EPFL), Lausanne, Switzerland
[6] Department of Physics and Materials Science, University of Luxembourg, 41 rue du Brill, L-4422
Belvaux, Luxembourg
[7] Synchrotron SOLEIL, Gif-sur-Yvette 91192, France
[8] SPEC, CEA, CNRS, Université Paris-Saclay, Gif-sur-Yvette, France
[9] Solid State Physics Institute, TU Wien, Vienna, Austria
[10] Center for Computational Quantum Physics, Flatiron Institute, New York, NY, United States of America
[11] Collège de France, 75005 Paris, France
[12] Centre de Physique Théorique, Ecole Polytechnique, CNRS, 91128 Palaiseau Cedex, France
[13] Department of Physics, Columbia University, New York, NY, United States of America

E-mail: jfowlie@stanford.edu

CrossMark

Abstract

Thin films of the solid solution $Nd_{1-x}La_xNiO_3$ are grown in order to study the expected 0 K
phase transitions at a specific composition. We experimentally map out the structural, electronic
and magnetic properties as a function of x and a discontinuous, possibly first order,
insulator–metal transition is observed at low temperature when $x = 0.2$. Raman spectroscopy
and scanning transmission electron microscopy show that this is not associated with a
correspondingly discontinuous global structural change. On the other hand, results from density
functional theory (DFT) and combined DFT and dynamical mean field theory calculations
produce a 0 K first order transition at around this composition. We further estimate the
temperature-dependence of the transition from thermodynamic considerations and find that a
discontinuous insulator–metal transition can be reproduced theoretically and implies a narrow
insulator–metal phase coexistence with x. Finally, muon spin rotation (μSR) measurements
suggest that there are non-static magnetic moments in the system that may be understood in the
context of the first order nature of the 0 K transition and its associated phase coexistence regime.

* Author to whom any correspondence should be addressed.

1. Introduction

A fundamental and very widely used tool of materials engineering is tofine-tune the chemical composition to achieve a specific property. Beyond this, families of materials with phase transitions are particularly interesting for applications as well as fundamental physics and the chemical composition often provides a control knob to set the transition at a desired condition, e.g. temperature or pressure.

The rare earth nickelates, RNiO$_3$, where R represents a rare earth or lanthanide element, comprise a family of perovskite oxides well-known for their metal-to-insulator transition (MIT). The fundamental structural motif is the corner-shared NiO$_6$ octahedron. The important Ni electronic states are the e_g ($d_{3z^2-r^2/x^2-y^2}$) doublet of the 3d shell, and formal valence considerations imply each Ni is in the 3^+ ionisation state with a d^7 electron configuration (one electron in the e_g multiplet). In fact, strong hybridisation and close level alignment of Ni-d and O-p states means that the Ni state is better approximated as $d^8\bar{L}$, corresponding to two electrons in the Ni e_g states and a hole shared amongst the nearby oxygens [1]. At high temperature the materials are metallic with a *Pnma* crystal structure in which all the Ni sites are equivalent (up to a rotation). As the temperature is decreased all of the nickelates except LaNiO$_3$ undergo a MIT [2, 3]. The insulating state is characterised by a $P2_1/n$ structure involving a two sublattice breathing distortion in which the mean Ni–O bond length alternates between a short and a long value. The lattice distortion is accompanied by a charge disproportionation which, from the point of view of fundamental many-body electronic structure theory should be treated as a hybridisation or site-selective order involving an alternating pattern of $d^8/d^8\bar{L}^2$ [4–6] but for most purposes may be thought of as a d^8/d^6 'charge order' corresponding to e_g^2 and e_g^0 respectively [7]. At low enough temperatures the insulating state is antiferromagnetic with a striped ordering pattern defined by a wavevector of $[\frac{1}{4},\frac{1}{4},\frac{1}{4}]$.

Because LaNiO$_3$ in bulk form remains metallic and non-magnetic with no two-sublattice breathing distortion down to lowest temperature, while NdNiO$_3$ has an insulating, lattice-distorted antiferromagnetic ground state, we expect that the solid solution Nd$_{1-x}$La$_x$NiO$_3$ will exhibit zero temperature insulator–metal, antiferromagnetic-paramagnetic and structural transitions for x between 0 and 1. If continuous (second order), a 'quantum' (zero temperature) phase transition may be expected to give rise to exotic behaviour [8]. In addition, LaNiO$_3$ forms in the $R\bar{3}c$ symmetry, distinct from the *Pnma* symmetry of NdNiO$_3$, so a composition-driven lattice symmetry transition must occur at a specific value of x that may

depend on temperature. This transition has been found to occur at around $x = 0.5$ at room temperature [9].

In this paper we present a comprehensive study of the composition-driven phase transitions occurring in Nd$_{1-x}$La$_x$NiO$_3$ as x is varied from 0 to 1. Our study uses a suite of films with a very dense set of x values allowing us to locate the transition with precision and determine the evolution of properties as the transition is approached. We perform transport, magnetic, light scattering and structural measurements as well as theoretical calculations. We find a zero temperature first order transition at a $x \approx 0.2$ between a low x $P2_1/n$ -symmetry (presumably lattice-distorted and charge-ordered) magnetic insulator and an intermediate x *Pnma* symmetry paramagnetic metallic state.

2. Sample preparation

The fully epitaxially strained Nd$_{1-x}$La$_x$NiO$_3$ films were grown by intermittent radio-frequency off-axis magnetron sputtering as described in section 7.

The substrates used are (LaAlO$_3$)$_{0.3}$(Sr$_2$AlTaO$_6$)$_{0.7}$ (LSAT), SrTiO$_3$ and NdGaO$_3$ all terminated in the (001) plane in pseudocubic notation. SrTiO$_3$, LSAT and NdGaO$_3$ provide biaxial strains of 1.7%, 0.8% and 0.5%, respectively, to LaNiO$_3$ and 2.5%, 1.6% and 1.3%, respectively, to NdNiO$_3$. This means that all substrates, for all Nd$_{1-x}$La$_x$NiO$_3$ compositions, should provide a tensile biaxial strain.

The films are, within our experimental resolution, homogenous solid solutions. The possibility that the solid solution is segregated into nanocomposites of NdNiO$_3$ and LaNiO$_3$ can be excluded. Indeed, figures 1(a) and (b) are compositional maps from electron energy loss spectroscopy (EELS) and energy dispersive x-ray spectroscopy (EDXS) showing that lanthanum and neodymium are homogeneously distributed down to the atomic scale.

3. Electronic and structural properties

The inset of figure 1(c) displays representative resistivity curves as a function of temperature for a set of 20 unit cell (u.c.) (=7.6 nm) thick Nd$_{1-x}$La$_x$NiO$_3$ with $x = (0, 0.1, 0.2, 0.3, 0.4, 0.6, 0.8, 1)$ on LSAT substrate. The films fall into four groups. As expected, the $x = 0$ (pure NdNiO$_3$) sample displays a clear MIT at around 150 K separating a high temperature, relatively poorly conducting, metallic state from a low temperature state with a very high resistance that grows exponentially as the temperature is decreased. The transition exhibits a hysteresis loop. The $x = 0.1$ and 0.2 Nd$_{1-x}$La$_x$NiO$_3$ have
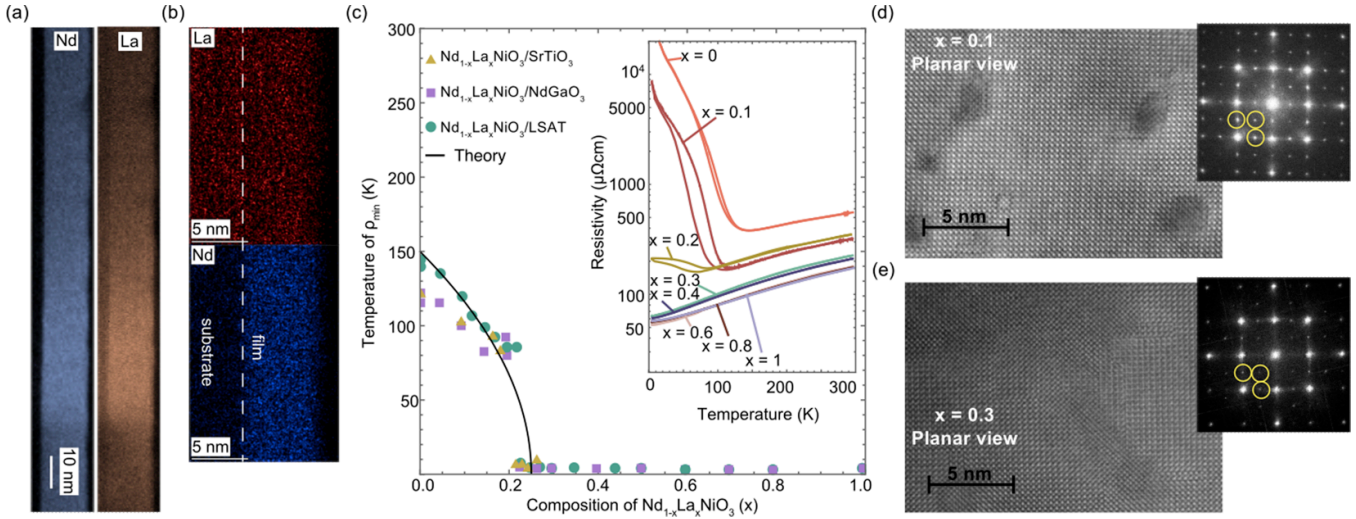
Figure 1. (a) Electron energy loss spectroscopy (EELS) images on the Nd (left) and La (right) M-edges for an $x = 0.4$ sample of 37 u.c. (=14 nm) red grown on LSAT. No secondary phases are observed. Note that thickness variations in the lamella cause a modulation in intensity that is the same for both Nd and La. (b) Energy dispersive x-ray spectroscopy (EDXS) showing the distributions of La (top) and Nd (bottom) for an $x = 0.25$ film of 16 u.c. (=6.1 nm) thickness on LSAT. Note that the A-site of the substrate contains 30% La so produces a similar signal to the film. (c) The temperature of the minimum resistivity, taken as the definition of the MIT temperature, for all the $Nd_{1-x}La_xNiO_3$ composition series on three substrates plotted against La fraction x. The black line is a theoretical result, discussed further in section 4. Inset: A representative set of resistivity curves as a function of temperature for $Nd_{1-x}La_xNiO_3$ on LSAT substrate. (d) and (e) High-angle annular dark-field (HAADF) images of planar view 40 u.c. (=15 nm) $Nd_{1-x}La_xNiO_3$ with $x = 0.1$ and $x = 0.3$ respectively. The insets are the fast Fourier transforms of the respective HAADF image with the half-order reflections identified by yellow circles.

metallic-state resistivities that are significantly lower than for $x = 0$ but similar between the two samples and higher than the ones with greater La content. They also show first order MITs albeit at lower temperatures than the $x = 0$ sample. The $x = 0.1$ film has an insulating state very similar to that of the $x = 0$ film, but with a lower resistivity. The low temperature state of the $x = 0.2$ film is classified here as insulating because the resistance exhibits a minimum at a non-zero temperature, but the low temperature resistivity is much lower than in the $x = 0.0$, 0.1 films and increases much less rapidly as $T \to 0$. Indeed at low temperature the conductivity of the $x = 0.2$ sample is $\approx 5000 \ \Omega^{-1} cm^{-1}$ which, using a Ni–Ni spacing of ≈ 0.4 nm is not much larger than the Mott 'minimum metallic conductivity' [10], suggesting that at this composition the material is only weakly insulating despite the relatively high temperature of the resistance minimum. We suggest that the low temperature resistivity of the $x = 0.2$ sample arises from a mixture of insulating and metallic domains, with the metallic domains not quite percolating. All the further samples are metallic in the sense of having a resistivity that increases with increasing temperature at all temperatures, but the metallic films fall into two groups, with $x = 0.3, 0.4$ having very similar resistivities that are noticeably higher than the resistivities of the larger-x films.

The main panel of figure 1(c) presents, as a function of x, the temperature at which the resistivity of each film (recorded on warming) is minimal for all the measured compositions on the three substrates. On the low x side of the plot, the points correspond to the MIT and the temperature of the transition decreases gradually with increasing La content. On the high x side the resistivity is clearly metallic with a resistance

that is minimised at $T = 0$. We may therefore approximately interpret this panel as a metal–insulator phase diagram, separating a low-T and low-x insulating regime from a high-T/high-x metallic regime defined by $d\rho/dT > 0$. However we must bear in mind that first order transitions are generically characterised by regions of phase coexistence, corresponding here to domains of insulating and metallic behaviour, so that some of the region with $T_{MI} = 0$ may correspond to a region of phase coexistence with percolating metallic domains while, as seen for the $x = 0.2$ sample, some of the regime with $T_{MI} \neq 0$ may correspond to a phase coexistence regime with non-percolating metallic regions. Thus, phase coexistence stemming from the first order nature of the transition with x provides an explanation for both the absolute resistivities (e.g. the weakly insulating behaviour for $x = 0.2$) and the discontinuous behaviour of the temperature of the minimum of resistivity.

The precise location of the microscopically defined phase boundary is therefore subject to some uncertainty. Comparison of the main panel of figure 1(c) with data previously reported for bulk solid solutions [11] suggests that the MIT in these films occurs at a somewhat lower x and lower T with respect to bulk, similar to films under compressive strain [12]. As an example, bulk $Nd_{1-x}La_xNiO_3$ with $x = 0.3$ is still insulating at low temperature with $T_{MI} = 110$ K [11].

Given the strong correlation between the lattice and electronic degrees of freedom in the rare earth nickelates, the MIT is expected to be strongly influenced by the structure. The difference in symmetry between the *Pnma* structure of room temperature $NdNiO_3$ and the $R\bar{3}c$ structure of $LaNiO_3$ is a natural candidate for the source of the first
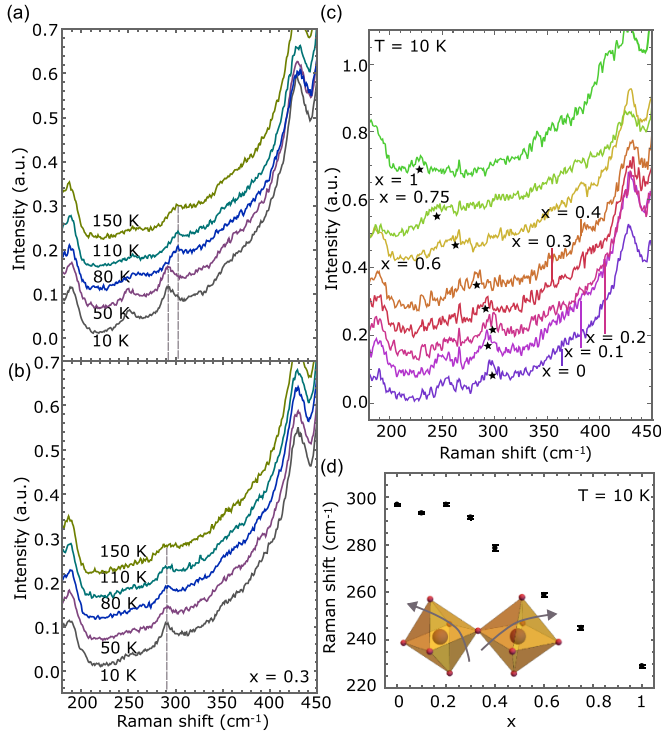
Figure 2. (a), (b) Raman spectra at various temperatures for 50 u.c. (=19 nm) thick $Nd_{1-x}La_xNiO_3$ on LSAT substrate with $x = 0.1$ (a) and $x = 0.3$ (b). The A_g mode is marked by a dashed line and is seen to shift, indicating a transition, for $x = 0.1$ only. (c) Raman spectra at 10 K for 50 u.c. (=19 nm) films on LSAT ranging from $x = 0$ to $x = 1$. The A_g mode is marked by stars. (d) The frequency of the A_g mode plotted as a function of x. Error bars indicate one standard deviation from a Lorentzian fit. A sketch of the structural distortion corresponding to this mode is shown in the inset.

order transition. However, our structural measurements rule out this scenario. Figures 1(d) and (e) show room temperature high-angle annular dark field (HAADF) images from scanning transmission electron microscopy for $x = 0.1$ and $x = 0.3$ $Nd_{1-x}La_xNiO_3$ prepared in a planar view. There is no noticeable change in the microstructure between the composition that becomes insulating (d) versus the one that remains metallic (e). Moreover, the fast Fourier transform patterns generated from these images, and displayed as insets, show that both films are in the *Pnma* symmetry by the presence of additional half-integer reflections, highlighted by yellow circles. Thus the change in symmetry from *Pnma* to $R\bar{3}c$ with increasing x must occur at an x that is larger than $x = 0.3$. Indeed, previous work found that the room temperature crossover in symmetry from *Pnma* to $R\bar{3}c$ with increasing x in the $Nd_{1-x}La_xNiO_3$ phase diagram occurs at approximately $x = 0.5$ [9].

The known strong association of lattice distortions and the MIT in the nickelate materials means that we can use the temperature-dependent Raman scattering spectra shown in figures 2(a) and (b) to bound the region of phase coexistence and therefore the x at which the MIT occurs. Panel (a) shows spectra taken on a $Nd_{1-x}La_xNiO_3$ with $x = 0.1$, which undergoes the MIT and, therefore, is assumed to also

undergo the *Pnma*-$P2_1/n$ symmetry lowering. The peak at ≈300 cm^{-1} arises from an A_g-symmetry phonon that is related to rigid antiphase rotations of corner-connected oxygen octahedra [13, 14]. This peak undergoes a clear frequency shift as the temperature is tuned across the temperature of the resistance minimum for this sample (≈100 K). There is no evidence of the low-frequency peak in the high-T data and no evidence of the high-frequency peak in the low-T data, strongly suggesting that at this x the sample completely transforms symmetry without significant phase coexistence. Similarly, for $x = 0.3$ (b), which remains metallic, only one peak is evident at all temperatures, again suggesting a single-phase sample.

Figure 2(c) shows the Raman spectra at 10 K for different compositions. The A_g mode frequency is marked with stars and then plotted as a function of composition x in panel (d) with error bars corresponding to one standard deviation from a Lorentzian fit. A change of slope is observed at around $x = 0.2$, reinforcing the conclusion that there is a change of space group at the same composition as the insulator–metal transition.

This sudden suppression of the MIT, which has been resolved in large part due to the high number of samples analysed, obscures the potentially-tunable quantum phase transition that was expected and cannot be explained by chemical or electronic phase separation.

For instance, a discontinuous change of bandwidth upon undergoing the symmetry crossover to $R\bar{3}c$ may occur at higher x but cannot account for the rapid suppression of the MIT at lower lanthanum content, this phenomenon manifesting within the *Pnma* phase only.

4. Theory

In this section we present a theoretical analysis. Extensive previous work has documented an intimate interplay between lattice/structural and electronic properties across the broad family of rare earth nickelates and confirmed in particular the importance of the Ni–O–Ni bond angle [15–21]. As observed in earlier work [9], the A_g-like modes of $Nd_{1-x}La_xNiO_3$ both soften as the La content is increased, demonstrating that the oxygen octahedral rotations decrease in magnitude. With the reduction of octahedral rotations comes a straightening of the Ni–O–Ni bond angle. We use the combination of density functional theory (DFT) and dynamical mean field theory (DMFT) to investigate the structural evolution and its impact on the electronic behaviour.

We perform bulk calculations (as described in [22]) and analyse—as described in [18]—DFT and DFT+DMFT calculations for $NdNiO_3$ and $x = 0.25$ $Nd_{1-x}La_xNiO_3$, in order to compare with the parameters obtained for $NdNiO_3$ previously benchmarked for these references. We use the $NdNiO_3$ DFT-relaxed structure and parameters from said previous references and approximate the randomly alloyed $Nd_{1-x}La_xNiO_3$ $x = 0.25$ compound by employing a 20-atom unit cell with three Nd and one La (note that any location for the novel La atom is equivalent by symmetry, therefore a single structure need only be considered). As before, the functional used is the Perdew–Burke–Ernzerhof [23], as it leads to structures with nearly identical bond angles to the experimental ones,

with our DMFT calculations very sensitive to these results. We then generate structurally disproportionate structures, as previously shown in [22], to extract the parameters g and k, which are the electron-lattice coupling and lattice stiffness respectively. After DFT relaxation, the average bond angle for the DFT-relaxed NdNiO$_3$ is 156.3° in-plane, and 157.1° out-of-plane. For the $x = 0.25$ structure, the average bond angle is 157.5° in-plane and 157.8° out-of-plane. This slight straightening is qualitatively consistent with our experimental observations and also with our expectations given the RNiO$_3$ bulk phase diagram.

We then select interaction parameters following [22] and, then, following [18] perform DFT plus DMFT calculations of the electronic charge disproportionation ΔN for a series of structures that interpolate between the DFT-relaxed *Pnma* structure and fully distorted $P2_1/n$ structure. We fit the results to the free energy functional:

$$F(\Delta N, Q) = \frac{1}{2}kQ^2 - \frac{1}{2}gQ\Delta N + F_{\mathrm{el}}(\Delta N) \qquad (1)$$

with:

$$F_{\mathrm{el}}(\Delta N) = \frac{1}{2}\chi_0^{-1}\Delta N^2 + \frac{1}{4}\beta\Delta N^4 + \frac{1}{6}\gamma\Delta N^6 \qquad (2)$$

where Q denotes the amplitude of the lattice distortion that breaks the *Pnma* symmetry and the k and g are obtained from the DFT calculations as described in [22] and the parameters in F_{el} come from the DMFT calculations. Representative results are shown in table 1. Note that following the conventions of Georgescu *et al* [22] the free energy is per two Ni (i.e. per unit cell of the disproportionate structure). We observe that all of the parameters change modestly between $x = 0$ and $x = 0.25$. To study other x values we linearly interpolate.

Figure 3 shows the calculated free energy landscape in the plane of Q and ΔN for $x = 0.0$ (panel (a)) and $x = 0.25$ (panel (b)). The landscape is characterised by two minima, one at the *Pnma* structure $Q = \Delta N = 0$ and one at a relatively strongly distorted $P2_1/n$ structure $Q \approx 0.05$ Å and $\Delta N \approx 1$, connected by a sharply defined saddle point path. In this calculation, as x is changed from $x = 0.0$ to 0.25 the global minimum switches from the $P2_1/n$ structure to the *Pnma* structure, confirming a first order composition-driven transition at an x between 0 and 0.25.

For a different perspective on the calculation, we present in figures 3(c) and (d) cuts of the free energy along the line connecting the origin to the distorted minimum for a series of x. The first order nature of the transition is clearly evident. Comparison of the two panels shows that the precise location of the transition with x is sensitive to details (shown here are the results obtained for two values of the on-site exchange J), but the important features are robust.

We now consider the temperature dependence of the phase boundary, on the assumption that the insulating state is characterised by a large electronic gap and a low-temperature entropy arising mainly from spin waves and acoustic phonons, both of which give a free energy contribution $\sim T^4$ at low T. On the other hand the metallic state has an entropic contribution from
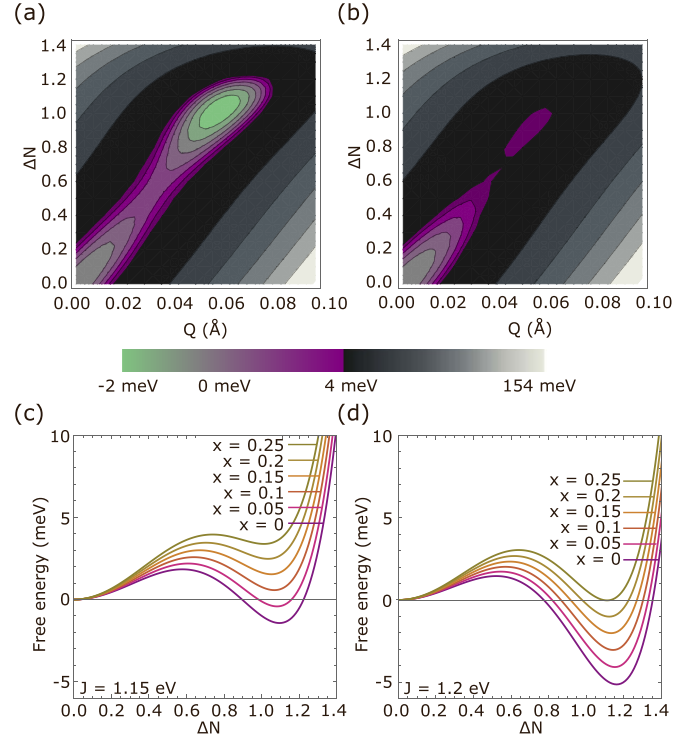

Figure 3. (a), (b) Two order parameter energy functional defined in equation (1) with the parameters found from DFT+DMFT as given in table 1 with $J = 1.15$ eV for (a) NdNiO$_3$ and (b) Nd$_{1-x}$La$_x$NiO$_3$ with $x = 0.25$. The two contour colour scales are selected to highlight the low energy behaviour and are provided underneath the plots. (c), (d) Line cuts of the free energy for $J = 1.15$ eV (c) and $J = 1.2$ eV (d). The parameters for $x = 0$ and $x = 0.25$ are obtained from DFT+DMFT and the parameters for the other compositions are linearly interpolated. Each line cut is defined along a vector from $Q = \Delta N = 0$ to the non-zero Q and ΔN that locally minimise the free energy for each x.

the Fermi surface $= AT^2$ where A is of the order of the inverse Fermi temperature determined by the effective mass. Neglecting the entropy of the insulating state, the metal–insulator free energy difference is then

$$F_{\mathrm{metal}} - F_{\mathrm{insulator}} \equiv \Delta F = E'(x_{\mathrm{c}} - x) - AT^2 \qquad (3)$$

with $E' = \partial E/\partial x$ the first derivative of the ground state energy with respect to x so that at very low T the phase boundary is given by

$$T_{\mathrm{MIT}}(x) = \sqrt{\frac{E'}{A}}\sqrt{x_{\mathrm{c}} - x}. \qquad (4)$$

The data in figure 3 yield $E' \approx 20$ meV uc^{-1} where the low temperature unit cell contains two Ni ions. To estimate A we note that DMFT calculations for the undistorted paramagnetic metallic state yield a mass enhancement $\lesssim 2$ while the bare density of states (summed over orbitals, spins and the two Ni sites in the unit cell) is about 12 eV^{-1}. The low temperature electronic specific heat coefficient is then given by $\pi^2/3$ times the density of states times the mass enhancement implying $A \approx 26$ eV^{-1}uc^{-1} so that we may estimate $T_{\mathrm{MIT}}[K](x) \approx 300\sqrt{x_{\mathrm{c}} - x}$. Thus the DMFT calculation suggests that the

Table 1. Parameters determined from DFT+DMFT that characterise the structural, electronic, and electron-lattice coupling of the free energy of $NdNiO_3$ and $Nd_{0.75}La_{0.25}NiO_3$ using both $J = 1.15$ and $J = 1.2$.

$Nd_{1-x}La_xNiO_3$	J (eV)	k(eV Å^{-2})	g(eV Å^{-1})	χ_0^{-1}(eV)	β (eV)	γ (eV)
$x = 0$	1.15	31.4298	3.4669	0.1199	−0.0931	0.0608
$x = 0.25$	1.15	32.0314	3.4697	0.1292	−0.099	0.0631
$x = 0$	1.2	31.6914	3.2212	0.1049	−0.1022	0.0631
$x = 0.25$	1.2	32.0314	3.2089	0.1137	−0.1083	0.0659

ordering temperature would rise from zero to the observed $x = 0.1$ value ≈ 70 K in an x range of about 0.05. It is reasonable that randomness near a first order transition could produce a coexistence regime of this size. Choosing a critical $x_c = 0.25$ yields the $T_{MIT}(x)$ curve shown as a black line in panel (c) of figure 1, which is in reasonable agreement with the experimental data.

5. Magnetic properties

Antiferromagnetism and the MIT are strongly linked in $NdNiO_3$ but antiferromagnetism is difficult to probe in thin films. In this section we report results of resonant soft x-ray scattering (REXS) and μSR probes of magnetism in our films. REXS reveals coherent long-ranged antiferromagnetic ordering via emergence of a Bragg scattering peak at the ordering wavevector. μSR reveals short-ranged magnetic ordering, fluctuating moments, and can give information on the magnetic volume fraction.

5.1. Probes of magnetic properties

5.1.1. Resonant x-ray scattering. REXS is a probe of long-range order. REXS [24] was carried out at the pseudocubic $\left[\frac{1}{4}, \frac{1}{4}, \frac{1}{4}\right]$ diffraction condition while the beam energy was set to resonate with the Ni L_3 edge at 853 eV. At low temperatures, a peak is observed that has been ascribed to the antiferromagnetic order of the nickel sublattice [25]. Here, this same peak was recorded in a series of symmetric θ–2θ scans from 40 K up to room temperature with the incident beam π-polarised. The maximal intensity of each of these scans for a 100 u.c. (= 38 nm) sample of $Nd_{1-x}La_xNiO_3$ with $x = 0.1$ on LSAT substrate is plotted as orange squares in figure 4(a) normalised to the low temperature value. As can be seen, the intensity of this peak drops sharply at the same temperature as the sample becomes metallic (resistivity plotted in black).

The full width at half-maximum of the resonant diffraction peak at low temperature is 2.34°, which, at this Bragg angle and x-ray wavelength, corresponds to a (0 0 1) coherence length of 100 u.c., precisely in agreement with the thickness of the film. This confirms that, at low temperature, the magnetic order is coherent across the entire film with no extra broadening from in-plane grains.

5.1.2. Low energy μSR. μSR is a well-demonstrated probe of local magnetic moment [26]. By decreasing the muon beam energy down to 4 keV, the mean stopping depth is

reduced to around 20 nm for materials such as $Nd_{1-x}La_xNiO_3$ with a density of around 7 gcm^{-3} according to Monte Carlo simulations [27]. Using low energy muons, therefore, maximises the sensitivity to the thin film. Low energy μSR [28] was carried out on a series of 100 u.c. (≈ 38 nm) thick $Nd_{1-x}La_xNiO_3$, on LSAT substrate. Each measurement, from 10 K up to room temperature, consists of at least two million events and was performed in a weak magnetic field of 10 mT applied transverse to the initial muon spin polarisation. The muon acts as a local magnetic sensor. There are two extremes for the case of an applied transverse magnetic field: 1. The muon spin ensemble experiences dominantly the applied field because it is much stronger than any internal field. In this case the muon spin precession is around the applied field with the maximal asymmetry amplitude. 2. The local static magnetic field distribution at the muon site is comparable to or stronger than the applied field: in this case the muon spin ensemble dephases very rapidly. Therefore, the asymmetry amplitude of the resulting muon spin precession is taken to be proportional to the non-magnetically-ordered volume fraction of the sample.

5.2. Discussion of magnetic properties

Figure 4(a) shows different temperature-dependent behaviour of the same $Nd_{1-x}La_xNiO_3$ $x = 0.1$ sample when comparing the REXS intensity to the magnetic volume fraction determined from μSR. The REXS shows a sharp transition at the same temperature at which the sample undergoes the MIT. On the other hand, μSR shows a gradually increasing magnetic volume fraction that begins when the sample is still in the metallic phase and does not reach 1.0 even at 10 K. Figure 4(b) shows that a similar broad onset of the magnetic volume fraction is observed in other compositions of $Nd_{1-x}La_xNiO_3$ with $x \neq 0$. These differences may be reconciled by considering that muon relaxation samples the system on a microsecond time scale while x-ray scattering occurs within picoseconds. In particular, either there are local magnetic moments that increase in density towards lower temperatures or the spin–spin correlation function increases, which decreases the fluctuation rate of the electronic moments into the MHz regime, quasi-static for the muons. Super-MHz fluctuation of local moments at higher temperatures would thus give rise to this behaviour.

Further evidence for fluctuating local moments is provided by figure 5(a). In the case of a static magnetic order, the μSR asymmetry should decay rapidly to a flat tail. The slow ZF-μSR decay observed here is typical of fluctuating systems.
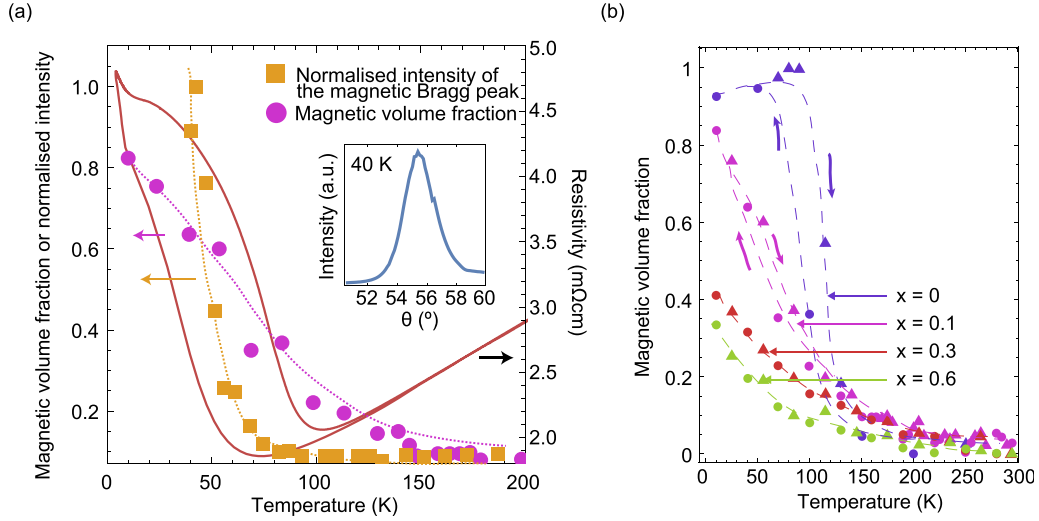
Figure 4. (a) For a 100 u.c. ($=$38 nm) thick $Nd_{1-x}La_xNiO_3$ with $x = 0.1$ on LSAT substrate, the resistivity (right axis) is displayed along with the intensity of the resonant magnetic Bragg peak (left axis orange squares) and the magnetic volume fraction determined from μSR (left axis pink circles). The dotted lines are guides to the eye. The inset displays the π-polarised θ–2θ scan at 853 eV and 40 K. (b) Magnetic volume fraction, as determined from the muon spin rotation asymmetry, as a function of temperature for three compositions of $Nd_{1-x}La_xNiO_3$ on LSAT substrate and $NdNiO_3$ on $LaAlO_3$, all 100 u.c. thick. Measurements recorded upon cooling are represented by circles and upon warming by triangles. The dashed lines are guides to the eye.
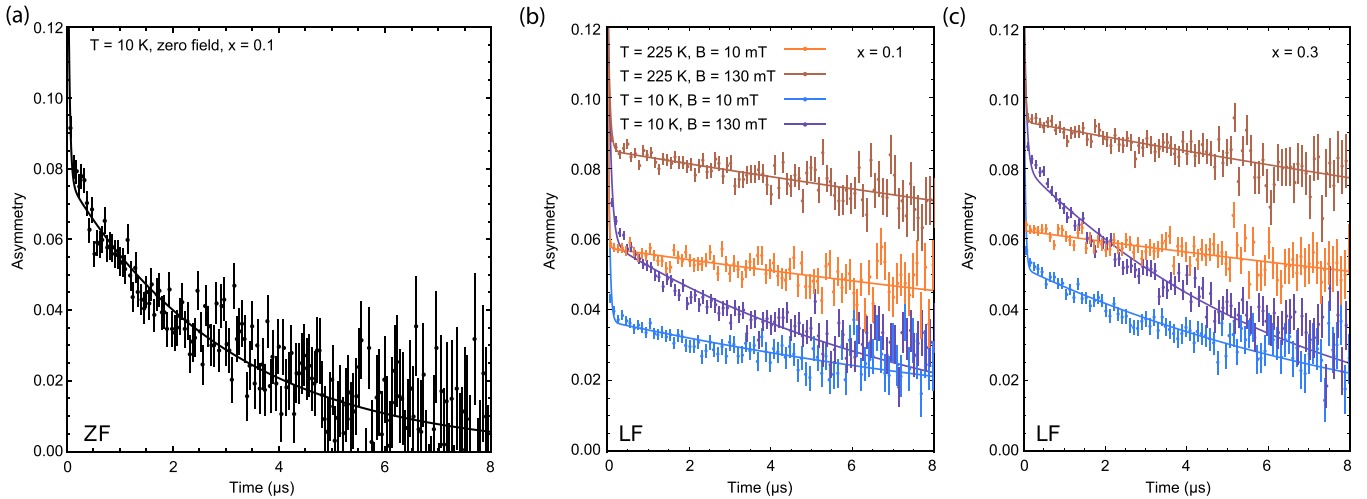

Figure 5. (a) Zero-field (ZF) muon decay spectrum of a sample of 100 u.c. thick $Nd_{1-x}La_xNiO_3$ with $x = 0.1$ at 10 K. The solid line is an exponential decay function. (b) and (c) The 10 K and 225 K muon decay asymmetry as a function of decay time for the $x = 0.1$ (b) and $x = 0.3$ (c) samples in a longitudinal field of 10 mT and 130 mT. The solid lines are exponential decay functions, $A_0 + A_1 e^{-\lambda t}$. The error bars correspond to one standard deviation of a Poisson distribution for each time bin. Note that the 10 mT and 130 mT LF asymmetries cannot be directly compared since, for technical reasons, they were measured under slightly different conditions.

Furthermore, the longitudinal field measurements shown in figures 5(b) and (c) demonstrate that the depolarisation is not quenched by the field, again indicative of fluctuating moments.

The origin of such fluctuations in $Nd_{1-x}La_xNiO_3$ is unknown. La^{3+} replaces Nd^{3+} so a background of cations with spin $\frac{1}{2}$ is gradually being diluted by cations with spin 0. Such a substitution may increase disorder in the insulating, antiferromagnetic state through fluctuating local moments. Previous μSR work on bulk (powder) $Nd_{1-x}La_xNiO_3$ shows a sharp transition in magnetic volume fraction that closely tracks the MIT [29]. Our samples may have amplified fluctuations due to the thin film nature of these crystals. Finally, it is possible

that fluctuations at higher x are related to small inclusions of insulating phase.

6. Conclusions

High quality epitaxial thin films of $Nd_{1-x}La_xNiO_3$ are synthesised. They are found to be chemically homogeneous. Both experimental evidence and theoretical results suggest a discontinuous (likely first order) transition between a low-x, low-T $P2_1/n$-symmetry insulating phase and a high-x high-T $Pnma$-symmetry metallic phase. Raman spectroscopy and

STEM analyses, show that this transport anomaly cannot be attributed to any *x*-dependent structural change in the material, consistent with previous work on bulk solid solutions. In particular, the transition between the *Pnma* symmetry of the high temperature phase of the $x = 0$ material and the $R\bar{3}c$ symmetry of the $x = 1$ end-member occurs at $x \approx 0.5$, far outside of the transition region [9]. This independence is also reflected in the effect of biaxial strain, which would be expected to renormalise any structural trend, but here does not have any influence on the behaviour with *x*.

The MIT, being first order, is likely to involve a region of phase coexistence near the transition point, driven e.g. by random variations in strain or local chemistry, for instance oxygen stoichiometry. The phase coexistence implies that the *transport* data do not necessarily provide the location of the thermodynamic phase transition, because once the metallic domains percolate, the resistivity is simply metallic. For example, the transport data at $x = 0.2$ reveal a resistivity with a minimum at ~ 70 K indicating a transition to an insulating state, but a low *T* conductivity not much larger than the Mott minimum metallic conductivity consistent with large but not percolating metallic domains. The Raman data however clearly indicate that the $x = 0.3$ sample has a negligible volume fraction of insulating phase at any *T*. We therefore suggest that the MIT occurs at a concentration *x* between 0.2 and 0.3 with the precise location masked by phase coexistence effects.

The magnetic data reported in section 5 are broadly consistent with this interpretation. The REXS and muon data on the $x = 0.1$ sample reveal an almost complete coherent magnetic volume fraction with the hysteresis characteristic of a first order transition while at $x = 0.3$ the muon data indicate a small volume fraction without any hysteresis, very similar to the observations at $x = 0$ and $T > T_{\mathrm{MIT}}$.

Theory also supports this picture. While the precise location of the critical *x* depends sensitively on parameters, the existence of a first order transition and the variation of the $T = 0$ insulator–metal energy difference with *x* are very robust features, insensitive to details. A simple analysis of the thermodynamics of the first order transition, based on the assumptions that the entropy of the insulating state is negligible and the metallic phase is only moderately correlated, produces a temperature-dependent phase boundary reasonably consistent with experiment.

Important directions for future research include direct detection of the coexisting phases for $x \approx 0.2$, determining the origin of the fluctuating magnetism observed even at large *x*, and refining the theory so that a more quantitative comparison to experiment can be made.

7. Methods

Films of $Nd_{1-x}La_xNiO_3$ were grown by intermittent radio frequency off-axis magnetron sputtering. The growth atmosphere was 7:2 $Ar:O_2$ at 0.18 Torr and the temperature was 450 °C.

For electrical resistivity measurements, the films were contacted by Al bonds onto sputtered Pt pads in a van der Pauw geometry [30] or on films etched into a Hall bar. The measurements were taken in a ^{4}He dipping station.

The STEM specimens were prepared by conventional methods, following mechanical tripod polishing and argon ion beam milling until electron transparency. Stacks of planar view HAADF images were acquired in a double-aberration-corrected FEI (Thermo Fisher Scientific) Titan Themis 60–300 microscope, located at the Interdisciplinary Centre for Electron Microscopy (CIME) in Ècole Polytechnique Fédérale de Lausanne (EPFL), operated at 300 kV using a convergence semi-angle of 20 mrad. The images of each stack were aligned with the SmartAlign plug-in for Digital Micrograph (GMS3.2), which corrects the image drift and the linear and non-linear scan distortions [31].

STEM-EELS spectrum image datasets were acquired with a Gatan GIF Quantum ERS spectrometer, using a collection semi-angle of $\simeq 47$ mrad. EDXS maps were acquired on the same microscope, using a four quadrant Super-X windowless silicon drift detector system and beam currents of around 100–250 pA. The maps were recorded and analysed using Thermo Fisher Scientiic Velox software.

The Raman spectra were acquired using an InVia Renishaw micro-Raman spectrometer, coupled with an Oxford HiRes microstat cooled with liquid He. Measurements were performed using the 633 nm line of a He–Ne laser. The spot size was around 1.3 μm in diameter. Polarised Raman data were acquired using a polariser, and no analyser after the sample due to the very low intensity of the signal. This results in the potential observation of all Raman-active symmetries in our spectra.

Data availability statement

Source data from DFT+DMFT is available at: https://github.com/alexandrub53/EnergyLandscapes. All muon spin measurements are available at musruser.psi.ch and can be found using the index in the main source data file.

The data that support the findings of this study are openly available at the following URL/DOI: https://purl.stanford.edu/hc677dr8144.

Acknowledgments

ORCID iDs

Jennifer Fowlie ⬡ https://orcid.org/0000-0002-3528-6390
Constance Toulouse ⬡ https://orcid.org/0000-0001-6060-8489
Nicolas Jaouen ⬡ https://orcid.org/0000-0003-1781-7669
Duncan T L Alexander ⬡ https://orcid.org/0000-0003-4350-8587

References

[1] Mizokawa T, Khomskii D I and Sawatzky G A 2000 Spin and charge ordering in self-doped Mott insulators *Phys. Rev.* B **61** 4

[2] Medarde M 1997 Structural, magnetic and electronic properties of RNiO$_3$ perovskites (R $=$ rare earth) *J. Phys.: Condens. Matter* **9** 1679

[3] Catalan G 2008 Progress in perovskite nickelate research *Phase Transit.* **81** 729

[4] Park H, Millis A J and Marianetti C A 2012 Site-selective Mott transition in rare-earth-element nickelates *Phys. Rev. Lett.* **109** 156402

[5] Johnston S, Mukherjee A, Elfimov I, Berciu M and Sawatzky G A 2014 Charge disproportionation without charge transfer in the rare-earth-element nickelates as a possible mechanism for the metal-insulator transition *Phys. Rev. Lett.* **112** 106404

[6] Bisogni V *et al* 2016 Ground-state oxygen holes and the metal-insulator transition in the negative charge-transfer rare-earth nickelates *Nat. Commun.* **7** 13017

[7] Subedi A, Peil O E and Georges A 2015 Low-energy description of the metal-insulator transition in the rare-earth nickelates *Phys. Rev.* B **91** 075128

[8] Pfleiderer C 2005 Why first order quantum phase transitions are interesting *J. Phys.: Condens. Matter* **17** S987–97

[9] Fowlie J, Mundet B, Toulouse C, Schober A, Guennou M, Domínguez C, Gibert M, Alexander D T, Kreisel J and Triscone J M 2021 Crossover between distinct symmetries in solid solutions of rare earth nickelates *APL Mater.* **9** 081119

[10] Mott N 1985 The minimum metallic conductivity *Int. Rev. Phys. Chem.* **4** 1

[11] Medarde M, García-Muñoz J L, Rosenkranz S, Granados X, Fontcuberta J and Lacorre P 1994 Crystallographic and magnetic study of Nd$_{0.7}$La$_{0.3}$NiO$_3$ *Physica* B **194–196** 367

[12] Disa A S, Kumah D P, Ngai J H, Specht E D, Arena D A, Walker F J and Ahn C H 2013 Phase diagram of compressively strained nickelate thin films *APL Mater.* **1** 032110

[13] Zaghrioui M, Bulou A, Lacorre P and Laffez P 2001 Electron diffraction and Raman scattering evidence of a symmetry breaking at the metal-insulator transition of NdNiO$_3$ *Phys. Rev.* B **64** 081102

[14] Gou G, Grinberg I, Rappe A M and Rondinelli J M 2011 Lattice normal modes and electronic properties of the correlated metal LaNiO$_3$ *Phys. Rev.* B **84** 144101

[15] Chen B *et al* 2021 Spatially controlled octahedral rotations and metal-insulator transitions in nickelate superlattices *Nano Lett.* **21** 1295

[16] Guzmán-Verri G G, Brierley R T and Littlewood P B 2019 Cooperative elastic fluctuations provide tuning of the metal-insulator transition *Nature* **576** 429

[17] Peil O E, Hampel A, Ederer C and Georges A 2019 Mechanism and control parameters of the coupled structural and metal-insulator transition in nickelates *Phys. Rev.* B **99** 245127

[18] Georgescu A B and Millis A J 2022 Quantifying the role of the lattice in metal-insulator phase transitions *Commun. Phys.* **5** 135

[19] Liao Z *et al* 2016 Controlled lateral anisotropy in correlated manganite heterostructures by interface-engineered oxygen octahedral coupling *Nat. Mater.* **15** 425

[20] Haule K and Pascut G L 2017 Mott transition and magnetism in rare earth nickelates and its fingerprint on the x-ray scattering *Sci. Rep.* **7** 10375

[21] Mercy A, Bieder J, Íñiguez J and Ghosez P 2017 Structurally triggered metal-insulator transition in rare-earth nickelates *Nat. Commun.* **8** 1677

[22] Georgescu A B, Peil O E, Disa A S, Georges A and Millis A J 2019 Disentangling lattice and electronic contributions to the metal-insulator transition from bulk vs. layer confined RNiO$_3$ *Proc. Natl Acad. Sci. USA* **116** 14434

[23] Perdew J P, Burke K and Ernzerhof M 1996 Generalized gradient approximation made simple *Phys. Rev. Lett.* **77** 3865

[24] Jaouen N, Tonnerre J M, Kapoujian G, Taunier P, Roux J P, Raoux D and Sirotti F 2004 An apparatus for temperature-dependent soft x-ray resonant magnetic scattering *J. Synchrotron Radiat.* **11** 353

[25] Scagnoli V, Staub U, Mulders A M, Janousch M, Meijer G I, Hammerl G, Tonnerre J M and Stojic N 2006 Role of magnetic and orbital ordering at the metal-insulator transition in NdNiO$_3$ *Phys. Rev.* B **73** 100409

[26] Dalmas de Réotier P and Yaouanc A 1997 Muon spin rotation and relaxation in magnetic materials *J. Phys.: Condens. Matter* **9** 9113

[27] Eckstein W 1991 *Computer Simulation of Ion-Solid Interactions* (Berlin: Springer)

[28] Prokscha T, Morenzoni E, Deiters K, Foroughi F, George D, Kobler R, Suter A and Vrankovic V 2008 The new μE4 beam at PSI: a hybrid-type large acceptance channel for the generation of a high intensity surface-muon beam *Nucl. Instrum. Methods Phys. Res.* A **595** 317

[29] Frandsen B A *et al* 2016 Volume-wise destruction of the antiferromagnetic Mott insulating state through quantum tuning *Nat. Commun.* **7** 12519

[30] van der Pauw L 1958 A method of measuring the resistivity and hall coefficient on lamellae of arbitrary shape *Phillips Tech. Rev.* **20** 220

[31] Jones L, Yang H, Pennycook T J, Marshall M S, Van Aert S, Browning N D, Castell M R and Nellist P D 2015 Smart align-a new tool for robust non-rigid registration of scanning microscope data *Adv. Struct. Chem. Imaging* **1** 8